SURFACE-DEPOSITED NIOBIUM OXIDE AND ORGANOSILANES IMPACT ON SILICON CHARGE-CARRIER LIFETIMES

Emma J. Pellerin
In partial requirements for the
Degree of Bachelor of Science, B.S. in Chemistry
submitted to the Faculty of

WORCESTER POLYTECHNIC INSTITUTE
100 Institute Road
Worcester, Massachusetts 01609

This report represents the work of WPI undergraduate students submitted to the faculty as evidence of completion of a degree requirement. WPI routinely publishes these reports on its website without editorial or peer review. For more information about the projects program at WPI, please see https://www.wpi.edu/project-based-learning.

Printed in the United States of America.

CONTENTS

LIST OF FIGURES

LIST OF TABLES

PREFACE

We studied the surface chemistry, energy band bending, and lifetime retainment of HF-etched intrinsic silicon wafers that received atomically deposited ultra-thin layers of Nb_2O_5 and surface derivatized (3,3,3–trifluoropropyl)trimethoxysilane. Nb_2O_5 has two main advantages; it passivates with fewer layers than other metal oxides and it's fermi energy levels are harmonious with those displaced by the development of native SiO_x on the surface. The (3,3,3-trifluorpropyl)trimethoxysilane was chosen to aid in the optimization of surface organic contacts for future tandem junction solar cell systems as attempted before by our group. The synthesis and forming gas annealing procedures for the Nb_2O_5 layers were outsourced and transferred from the Strandwitz group at Lehigh University, along with the sample's initial SRV measurements. Once received, samples were scanned by XPS to verify the quality of metal oxide on the surface and other applicable chemical species, samples were also scanned following silane derivatization to prove surface contacts created. TRMPS was utilized continuously to model changes in SRV and to understand what experiments contribute to those changes. While Nb_2O_5 layers demonstrated increased lifetime retainment, lifetimes decrease by 200–300 μs following silanization. This trend is measured over several months and is an overall increase compared to plain i-Si with native-grown SiO_x over the same time period, but elucidates the need for further investigation into silicon's surface environment.

ACKNOWLEDGMENTS

First and foremost I would like to extend my biggest gratitude to Professor Grimm who saw me through all the highs and lows of not only my research but my entire college career. My time at WPI was full of challenges and hurdles but Professor Grimm always supported me and taught me so many crucial lab and life lessons along the way. Everything I know I attribute to him. To Julia, I want you to know I truly look up to you so much. You taught me not only how to be a good colleague and friend but how to be a mentor to those around me. Thank you so much for all the break room chats and laughs in and out of the lab. Jocelyn, thank you for being my introduction to research and sharing your passion with me. You taught me so much about what it means to be a scientist and how to balance myself in the lab. I wish you the best at Caltech and beyond. Becca, Michelle, Abby, and Rebecca it has been an absolute pleasure to work alongside you guys and watch you all grow with me. I admire you all for your character and work ethic, you guys inspired me every day to push through my toughest points and grow as an individual, so thank you. To the rest of Grimmgroup I wish you luck in your endeavors in and after college, it was a pleasure to meet and work with all of you.

development events. The lessons and connections I gained from these experiences will stay with me through the rest of my professional career, so thank you.

A final thank you to my parents and step-parents for their continuous and neverending support while I am away from home pursuing my dreams. I know it hasn't been easy. To Kat and John, thank you for always being there for me and believing in me no matter what was going on in our lives. You guys are my biggest supporters and the reason I am still here today. I love you both so much.

I truly stand on the shoulders of giants, my achievements are not solely my own and I am beyond happy to share this amazing accomplishment with the people that have been with me through it all. Thank you.

<div align="right">E. J. P.</div>

GLOSSARY

GHG   Greenhouse Gas

ETL   Electron Transport Layer

HTL   Hole Transport Layer

TMO   Transition Metal Oxide

XPS   X-ray Photoelectron Spectra/Spectroscopy

UHV   Ultra-high vacuum

ALD   Atomic Layer Deposition

XRD   X-ray Diffraction

TRMPS   Time Resolved Microwave Photoconductivity Spectroscopy

FTO   Fluorine-doped Tin Oxide

CHAPTER 1

INTRODUCTION

1.1 A Global Energy Crisis

In 2020 alone the world emitted 34 billion tons of carbon dioxide (CO_2) from fossil fuels and we have yet to reach the peak, as emissions continue to grow every year.[1] The United States is responsible for 25% of historical emissions, having produced 400 billion tons since 1751.[1]

To fuel the rapid development of the modern world the exploitation of cheap nonrenewable energy sources is encouraged by those who stand to make a profit. Fossil fuels such as coal, petroleum, and natural gases are consumed at significant rates. The extensive rate of Greenhouse Gas (GHG) emissions, which consists of carbon dioxide (CO_2), methane (CH_4), chlorofluorocarbons (CFCs), and hydrofluorocarbons (HFCs) can be contributed to these nonre-newable sources of energy along with aerosols and over farming of cattle.[2] Due to these unsustainable habits, the Earth's average surface temperature has increased between 1.8 and 4 °C in the 21st century, the majority of which has occurred in the last seven years.[2] Since the 1970's scientists have begun to witness and consistently measure northern and southern ice sheets shrinking
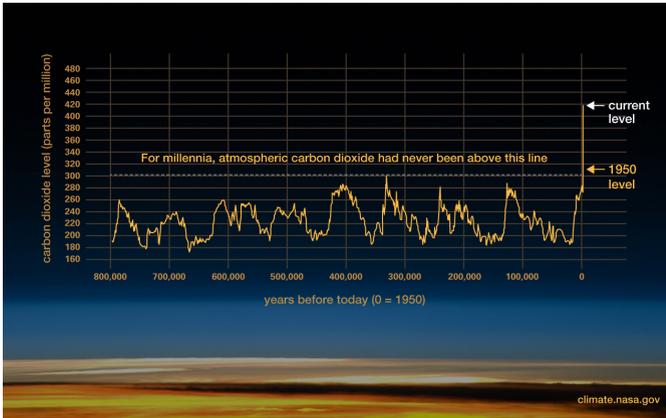
Figure 1.1. CO_2 levels in ppm vs the age of the Earth emphasizes the drastic change that has occurred in the last 100 years due to human-related activity. From https://climate.nasa.gov/evidence/.

due to ocean warming, which has concurrently raised the sea level making parts of the world unhabitable.[3,4] The Earth stores 90% of the extra energy in our atmosphere in the ocean; the stability of our biosphere is immensely dependent on its oceans.[3]

Now reports indicate that oceanic acidity has risen over 30%, this shift can easily annihilate thousands of important aquatic species that we depend on for survival.[3,4] Not to mention record-breaking hurricanes, forest fires, floods, and other natural disasters occurring every year. [3]

Extracting non-renewable energy sources and releasing GHGs from the Earth into the atmosphere has and will continue to rapidly deteriorate our environment. Modern trends in global climate change are not just due to the natural cycles of the planet but induced and worsened by the mining and usage of non-renewable energy sources as denoted in Fig.1.1. If we hope to stop this trend before it is too late, we must fund research into new sustainable energy sources. One of the significant challenges of modern-day society is determining a method of collecting and distributing large amounts of renewable energy, sustainably and ethically.

1.2 Prospective Sources of Renewable Energy

When investigating all feasible methods of energy collection and storage it is easy to see that no single path is without consequences. A thermodynamically perfect system is just not possible with our current technology, but some renewable sources certainly come very close. Solar energy, wind, and geothermal power are among those options. While wind and geothermal

sources can be beneficial and clean, their availability is limited by geographical location. This causes a loss in efficiency when attempting to distribute the charge over large areas. Solar methods are favorable because the Sun is always radiating somewhere on the surface of the Earth. After considering atmospheric scattering and absorption it can be calculated that about 80,000 TW of power reaches Earth's surface at any given moment from the radiation of the Sun.[5]

There are three actively researched ways to harness energy from the sun, solar-thermal, solar-chemical, and solar-electrical. Solar thermal methods produce chemical energy through the use of thermoelectric generators and other techniques, but the aspect of insulating the heat prevents this method from widespread applications. Solar chemical processes are observed all over the world in the form of photosynthesis. Synthetic applications of this are much simpler but not impossible, efficiencies are not as optimized as their natural correspondences. Pairing certain photovoltaic systems with the correct catalytic substances can have positive effects, but more research is necessary if these systems hope to be comparable to millions of years of evolution.[6] The final method and subject of focus of this research is the synthesis and passivation of solar electrical cells.

1.3   Current Research and Future Utilization of Photovoltaic Solar Cells

Solar cells directly convert solar energy into usable electrical charge. There are many varieties of cells from single cells to tandem-junction cells and several options of materials with varying bandgaps as well. All these characteristics can heavily impact the conversion efficiencies of the photovoltaic system. Overall, producing solar cells is not an environmentally intrusive process and what little waste is created is nowhere near the damage done by non-renewable sources. As seen in Table 1.1, semiconductors towards the bottom contribute 2% of the world's GHGs', but this is still the lowest out of all the sources.[2] While current forms of electricity distribution contribute 37% to CO_2 levels.[2] Several current iterations involve lead-based materials since they have the greatest conversion efficiencies, but when they inevitably break down they can cause damage to their surrounding environments. Research has shown that increased efficiencies are achievable sustainably by using other materials in a tandem-junction system.[6,7]

While materials for solar cells such as cadmium telluride (CdTe), gallium arsenide (GaAs), and copper indium gallium selenide (CIGS) are somewhat expensive and not as readily available as oil or coal, photovoltaic research has led to more reproducible alternatives. The driving force for widespread implementation is not only its sustainability but also the economic cost to society. Non-renewable sources tend to be cheaper but research and production of photovoltaics can create thousands if not millions of jobs not to

Table 1.1. Sources and percentage impacts of various greenhouse gases.[a]

Greenhouse gas	Source	Contrib. (%)
Carbon dioxide	Electricity	37
	Transportation	31
	Industry	15
	Residential, Commerical Areas	10
	Non-Fossil Fuel Combustion	6
Methane	Natural Gas and Petroleum	29
	Enteric Fermentation	26
	Landfills	18
	Coal Mining	10
	Manure Management	10
	Others	8
Nitrous oxide	Agricultural Soil Management	74
	Stationary Combustion	6
	Industry or Chemical Production	5
	Transportation	5
	Manure Management	5
	Others	4
Fluorinated gases	Substitution of O_3-Depleting Substances	90
	Electrical transmission, distribution	3
	Production, processing of Al and Mg	3
	HCFC-22 production	2
	Semiconductor manufacturing	2

[a] Table adapted from 10.1016/B978-0-12-822928-6.00005-8

mention the hundreds it could save families and companies annually on their electricity bills.[7,8]

The first generation of photovoltaic (PV) cells consisted of monocrystalline and polycrystalline silicon. Single cells reach efficiencies of 25% which are a bit greater than the 20.4% efficiency of tandem-junction cells but also cost more in manufacturing.[9,10] The second generation is where research began to
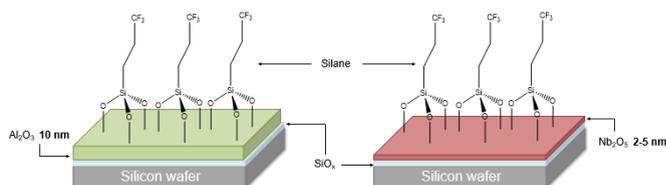
Figure 1.2. Aluminum oxide versus niobium oxide passivation thickness in tandem-junction with fluorine-terminated silane (3,3,3-trifluoropropyl)trimethoxysilane.

shift gears towards thin films. They use less material and therefore are more cost-effective. Cesium Titanium Bromide (Cs_2TiBr_6), is a large-grain material that was researched in this project (Appendix A). The third generation of PV cells resembles best the materials and procedures that are witnessed in this work. Reducing energy consumption by 50–80% as compared to the second generation.[6] Interweaving electron transport layers (ETLS) and hole transport layers can maximize conversion efficiencies as seen in recent 4-junction systems that reach up to 40%.[9] And with new synthesizes investigating flexible organosilane passivating layers and other cheaper and environmentally friendly materials, we will continue to see a rise in relevancy.[8,11]

1.4   Investigation of Surface Derivatized Organosilanes and Ultra-thin Layers of Niobium Oxide on Silicon

This specific project focuses on the implementation and passivation of Si(111) surfaces, which when implemented alone has verified efficiencies of around 25%.[10] The material exemplifies optimally low surface recombination velocities in aqueous solutions of $HF_{(aq)}$ and $H_2SO_{4(aq)}$ due to low trap state densities.[12] These conditions may be feasibly reproduced with the right surface conditions. The natural oxidation of the silicon wafers, defects, and other crystalline misalignments causes band bending, which increases trap states in the structure, ruining the material's ability to retain charge carriers. Passivation reduces interfacial recombination by mitigating those trap states.[10] Several metal oxides have been experimented with in hopes of passivating the surface from this phenomenon. ETLs such as silicon oxide (SiO_x), and silicon nitride (SiN_x), have been investigated but interlayer limits result in a reduction of charge carrier lifetimes.[13] Specifically, aluminum oxide (Al_2O_3) has been proven to fully passivate the surface of silicon samples with 10 nm, while retaining lifetime values of >1000 μs but it is too thick to pass charge through. Flexible organosilane layers such as Rylene-terminated molecules are also being pursued but surface sterics makes it difficult for secondary surface derivatization to occur after primary synthesis, ultimately killing surface lifetimes.[5]
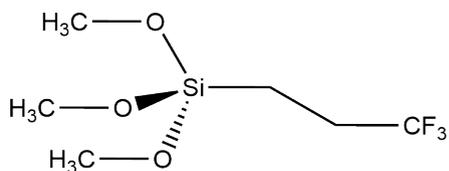
Figure 1.3. Structural formula of the (3,3,3-trifluoropropyl)trimethoxysilane before surface attachment.

In these experiments, we hope to combine both of these methods of passivation to successfully deposit niobium oxide (Nb_2O_5) in conjunction with (3,3,3-trifluoropropyl)trimethoxysilane, as seen in Fig. 1.3 and 4.1, to maintain the optimal lifetimes that we observe from pure silicon. This is exemplified in Fig. 1.2. Nb_2O_5 is a new area of transition metal oxides (TMOS) being explored that have the ability to not only passivate the surface but do so with ultra-thin layers that allow charge to be transferred readily. We hope to attain successful derivatization of organic layers apical of the surface-deposited ultra-thin Nb_2O_5 interlayers to verify passivation and observe consistent lifetime measurements of photogenerated charge carriers.

CHAPTER 2

BACKGROUND

Si(111) is a well-established semiconductor with charge-carrier lifetimes that are beneficial in a wide range of applications and a band gap of 1.2 eV.[5] Charged surface states cause the conduction and valence bands to bend within the crystal structure of the Si(111) due to the induced electric field.[11] This band bending phenomenon, shown in Fig. 2.1 is exacerbated by surface oxidation, both causing increased trap state densities at the surface. The phenomena of trap states cause surface recombination velocities to surge.[11,14] Several methods to reverse this band-bending effect and passivate the surface have been investigated in hopes of retaining the current efficiencies of Si(111) around 25%.[9] Lower surface recombination velocities (SRV) <1cm^{-1}, have been verified in Si(111) when in contact with strongly acidic solutions elucidating trap states within the structure.[11,12,14,15]

An awarded Ph.D. member of our group, Alexander D. Carl, explored the impacts that surface-derivatized organic layers would have on charge-carrier lifetimes and subsequently the SRV. He hypothesized that covalently-bound, organic monolayers of carrier-selective molecules would provide passivation and charge-carrier selectivity at semiconductor surfaces.[5] While the first
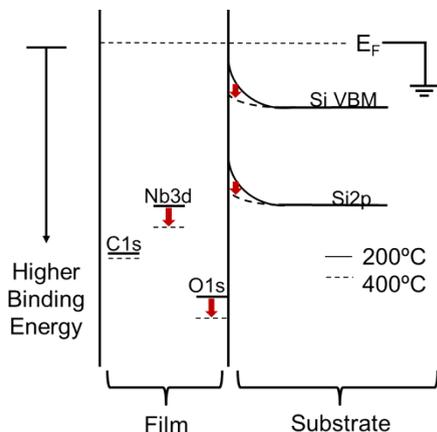
Figure 2.1. Band bending in substrate silicon, native grown surface carbon and oxygen and thin-film Nb_2O_5. Adapted from Fig. 6 in ref. 10.1063/5.0067281.

phase of surface derivatization showed promising results the bulky characteristics of the different Rylene-terminated molecules always yielded surface oxidation after attempting the second-degree derivatization.[5]

Metal oxide precursors are concurrently studied as ETLS for potential surface passivation. Compounds such as aluminum oxide (Al_2O_3) and silicon oxide (SiO_x) have been employed, with results indicating consistently complete surface coverage.[10,14] Unfortunately, due to the surface thickness required and/or differences in band alignment, passivation with these options impairs charge lifetimes. Recently more literature has been published describing the advantages of (tert-butylimido)-tris (diethylamino)-niobium [$(CH_3)_3CNNb(N(C_2H_5)_2)_3$, TBTDEN] ($Nb_2O_5$) as a precursor and H_2O as a reactant.[10,16] Literature establishes that Nb_2O_5 can passivate the surface on approximately the same level as published Al_2O_3 but in ultra-thin layers of 1–5 nm which still enable charge transfer. Defects that occur during the atomic layer deposition of the Nb_2O_5 are realigned when utilized in tandem with forming gas annealing procedures.[10,16]

In this project, we attempt to elucidate ways in which organic surface derivatization and passivation with TMOs may work in conjunction with one another to prevent different sourced trap states from causing premature surface recombination. This will be executed through out-sourced atomic layer deposition and forming gas annealing experiments of ultra-thin Nb_2O_5 on RCA–1 and 2, and HF-cleaned intrinsic silicon by Lehigh University. These samples will then undergo surface-derivatization by fluorine-terminated organosilanes with continuous measurements of microwave photoconductivity through-

out to verify surface recombination velocities and photogenerated charge-carrier lifetimes.

CHAPTER 3

EXPERIMENTAL

3.1 Materials and Chemicals

Several different chemicals were used as received by the manufacturer, in both the preparation and synthesis of silicon substrates. All of these were used as received unless otherwise noted. Double-sided polished intrinsic (111) (ρ > 3,000 Ω cm^{-1}) silicon wafers (i–Si) were the substrates utilized for the majority of data collection. Radio Corporations of America solutions one and two (RCA–1, RCA–2)were used for sample cleaning and preparation. The DI water that was used was Ultra-high purity (UHP) water obtained through a Milli-Q filtration system, which provided 18M Ω cm resistivity (Millipore). RCA–1 consisted of 6 parts DI water, 1 part ammonium hydroxide (NH$_4$OH, 28–30%, Acros Organics), and 1 part hydrogen peroxide (H$_2$O$_2$, 29–32% aqueous solution, Alfa Aesar). RCA–2 was also 6 vol. parts DI water, 1 part concentrated hydrochloric acid (HCl, ACS plus, Fisher Chemicals), and 1 part H$_2$O$_{2(aq)}$. A piranha solution was 1 part H$_2$O$_2$, Fisher Chemicals). *Caution:* piranha solution is a strongly oxidizing acid that reacts violently and exothermically with organic matter. Use appro-

priate safety measures for handling and disposal. Hydrofluoric acid (HF, 80–90%, Cirtec) was diluted to 0.1% for handling safety. Ethanol (anhydrous, histological grade, Fisher), and isopropyl alcohol (IPA, C_3H_8O, 99.6%, Acros Organics) was used as received. Acetic acid (HAc, $C_2H_4O_2$, Certified ACS, MFG) was diluted in ethanol to 0.1 M. Toluene (C_7H_8, 99.85% extra-dry, Acros Organics, further stored over activated molecular sieves). Molecular sieves (3Å, 1–2 mm beads(0.04-0.08in), Alfa Aesar) were directly activated prior to use via flame drying on a diffusion-pumped Schlenk line with a base pressure below 1×10^{-3} Torr. Silanization experiments utilized (3,3,3-trifluoropropyl)trimethoxysilane (97%, Thermo Scientific) that was diluted to 10 mM in toluene.

3.2   Experimental Procedure

3.2.1   Silicon Wafer Preparation

The intrinsic silicon (i–Si) wafers were cut to a size of 2×2 cm^2 in area to achieve ideal surface recombination velocities. Silicon wafers were cleaned by submerging them in RCA–1 solution in borosilicate glass tubes. The wafers and solution were heated to ~80 °C for 10–15 minutes and then rinsed with UHP DI water. The same process was then repeated following the RCA–1 but with RCA–2. After samples were cleaned with the RCA solutions, they were etched with HF by pipette drops on both sides. After, samples were rinsed with more UHP DI water, dried, packaged, and sent to the Strandwitz research group at Lehigh University lab for niobium oxide and aluminum oxide passivation atomic layer deposition and annealing.

3.2.2   Atomic Layer Deposition (ALD)

Two batches of i–Si wafers were sent to Lehigh University for metal oxide precursor passivation. The first batch consisted of five samples and the second consisted of ten. The second batch will be the subject of all pertinent research. Out of the ten, five originated at Lehigh and the other five originated at WPI. Table 3.1 specifies which samples received which metal oxide, the number of layers on the surface in nanometers, and the initial lifetime data.

The Lehigh samples were also cleaned with the standard RCA recipes then proceeded with deposition of the (*tert*-butylimido)-*tris*-(diethylamino)-niobium (TBTDEN) precursor on the surface for all samples. Once the samples received Nb_2O_5 or Al_2O_3 surface passivation they were sent back to our lab for further organosilane surface derivatization, XPS characterization, and lifetime studies.

Table 3.1. Intrinsic silicon wafer characterization and lifetime values, before and following an annealing procedure at Lehigh University. The final two columns, "WPI received" and "One month later" respectively represent lifetime values acquired directly following receipt at WPI from Lehigh, and after a one-month pause.

Sample ID	Origin	Metal Precursor	Pre-anneal τ (μs)	Post-anneal τ (μs)	WPI received τ (μs)	One month later τ (μs)
1	Lehigh	10 nm Al_2O_3	5	120	163	288
2	Lehigh	2 nm Nb_2O_5	136	154	175	791
3	Lehigh	2 nm Nb_2O_5	73	122	132	985
4	Lehigh	2 nm Nb_2O_5	73	121	157	1036
5	Lehigh	2 nm Nb_2O_5	93	107	199	666
6	WPI	10 nm Al_2O_3	4	605	147	897
7	WPI	2 nm Nb_2O_5	27	72	107	509
8	WPI	2 nm Nb_2O_5	28	57	835	513
9	WPI	2 nm Nb_2O_5	40	59	559	533
10	WPI	2 nm Nb_2O_5	31	53	445	594

Table 3.2. Wafer identification along with silane recipes, concentration and reaction time. All reactions were with (3,3,3–trifluoropropyl)trimethoxysilane.

Sample #	Metal Oxide	Concentration (mM)	Reaction Duration (h)
1	10 nm Al_2O_3	1	2
4	2 nm Nb_2O_5	10	6
6	10 nm Al_2O_3	10	6
7	2 nm Nb_2O_5	2	24
8	2 nm Nb_2O_5	2	6
9	2 nm Nb_2O_5	10	6
10	2 nm Nb_2O_5	2	6

3.2.3   Organosilane Surface Derivatization

Before silane was deposited measurements were retaken on the lifetime (τ) and the surface recombination velocities (SRV) of all samples. This procedure is reported in §3.3.2 regarding microwave photoconductivity data collection. Throughout experimentation, necessary parameters were altered to not only achieve deposition of silane on the surface but to do so without destroying the lifetimes of the silicon. The recipe Table 3.2 was the achievable progress within the scope of this project. The samples chosen had the best original lifetime values and therefore were chosen for further silane experimentation.

The recipes completed on samples 4, 6, 8 and 9 produced the best results in both fluorine peak areas and lifetime retainment and will be reported in more detail here. The sample, a 50 mL plastic centrifuge tube, a 3 mL plastic pipet, tweezers, a 10 μL micropipette (Gilson Pipetman), and sanitary tips were pumped down into the lab's constant nitrogen flow flush box.

For samples 4, 6, and 9, 10 mL of super-dry toluene was pulled from a stock solution created and stored in the flushbox and dispensed into the 50 mL centrifuge tube. 19.11 μL of the (3,3,3-trifluoropropyl)trimethoxysilane was measured and dispensed into the centrifuge tube as well. For 7, 8, and 10, 10 mL of the toluene stock solution was used then 3.82 μL of the silane. The sample was then carefully placed in the centrifuge tube and the system was capped. All samples except the first received and acetic acid work up dispensed on the bench. 10 mL of the 0.1 M acetic acid, ethanol stock solution was measured and placed in the centrifuge tube which was then attached to a bench-top sonicator to react for 1 hour. After an hour had passed the sonicator was shut off and the system was left to react for another 5 hours.

Once fully reacted the solution was decanted into a beaker with a glass funnel, carefully, so that the sample was not dropped or scratched. Ethanol via a squirt bottle was added to the centrifuge tube so that the wafer was completely submerged in the solvent. The system was left uncapped while sonicating for 5 minutes, then decanted again. The wafer was then submerged in IPA via a squirt bottle and sonicated again for another 5 minutes. After the workup was completed the sample was dried via an argon gun and taken back to the Microwave photoconductivity spectrometer for SRV verification.

3.3 Data Collection

The main two forms of data collection utilized were X-ray photoelectron spectroscopy (XPS) and time-resolved microwave photoconductivity spectroscopy (TRMPS). The next two sections specify how these techniques were used on the samples to collect data and how the data was formatted for further surface investigation.

3.3.1 X-ray Photoelectron Spectroscopy (XPS)

A PHI 5600 XPS system that utilizes a third-party data acquisition system (RBD Instruments) captured all the photoelectron spectra that are detailed in this report. The analysis chamber was constantly being pumped on by an ultra-high vacuum turbo pump resulting in base pressures $<1 \times 10^{-9}$ Torr. Photoelectrons were collected by a hemispherical energy analyzer that is positioned at 90° with respect to the incoming monochromated Al K_α X-radiation. XPS data collection employed a stage that yields 45° angles both for the incoming X-rays and for the photoelectron take-off angle with respect to the sample normal angle. The apparatus structure is detailed in Fig. 3.1.

All samples were scanned to capture wide-energy surveys and high-resolution multiplex spectra. The survey spectra utilized a 117.40 eV pass energy, 0.5 eV step size, and a 0.05 s dwell time per step. The multiplex spectra employed a 23.5 eV pass energy, 0.05 eV step size and 0.05 s dwell time per step covering the Si 2p, Nb 3d, O 1s, C 1s, F 1s, Al 2p, and N 1s regions.

First, the stainless steel puck, screw, and copper tab were rinsed with IPA. Then, the sample was mounted to the puck with a copper tab making contact at the corner of the wafer, taking up as little surface area as possible while making sure the sample is secure. The puck would then be loaded into the antechamber where the rough pump would be used to evacuate the pressure of the system <250 milliTorr. The rough pump would then be isolated and the antechamber would be switched over to the turbo pump where it would continue evacuation for another hour. Once the antechamber and the analysis chamber are comparable in pressure, the puck can then be transferred into the UHV chamber for sample scanning.
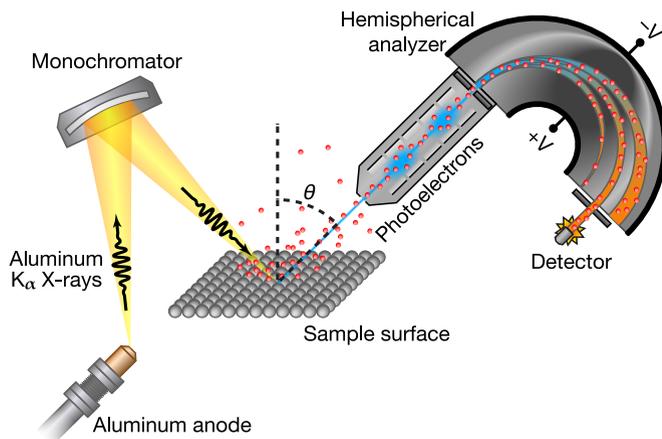
Figure 3.1. X-Ray Photoelectron Spectrometer. Image credit, Dr. Julia L. Martin.

Post-acquisition fitting utilized the peak fitting program XPSCasa. Data fitting employed baseline-corrected, pseudo-Voigt, GL(x)-style functions where x nonlinearly scales from a pure Gaussian ($x = 0$) to a pure Lorentzian ($x = 100$). Baseline functions were either of a Linear type, a Shirley type, or a Tougaard style with $B = 2900$ eV^2 and $C = 1643$ eV^2 within a universal function that is scaled to the height of the photoelectron data. The Si 2p doublets were fit with a linear baseline. The doublet was fit with three 2p$_{1/2}$ peaks and three 2p$_{3/2}$ peaks. Si 2p doublets were constrained to have identical full-width-at-half-max (fwhm) with the 2p$_{1/2}$ peaks containing 50% of the area of the 2p$_{3/2}$ peaks with a spin-orbit-splitting energy of 0.61 eV. The Al 2p region was fitted with a linear baseline with one unconstrained fitting feature. The Nb 3d regions utilized a Tougaard baseline with a spin-orbit-splitting of 2.72 eV, mutually identical fwhm values, and area constraints, and the 3d$_{3/2}$ peak area was constrained to be $\frac{2}{3}$rds that of the 3d$_{5/2}$ peak. There were several peaks in the C 1s region above a linear baseline from both silane features and adventitious contaminants. All features within the C 1s region utilized identical fwhm values to reduce the likelihood of mathematically optimized but chemically unrealistic width values. The O 1s region utilized a Tougaard baseline with metal-oxide-ascribable features at 529–531 eV, and adventitious-organic-ascribable features at 531–533 eV. We did not constrain fwhm values between oxide-ascribable and organic-ascribable O 1s features. One unconstrained GL(30) fitting feature well described the F 1s region above a linear background.[17]
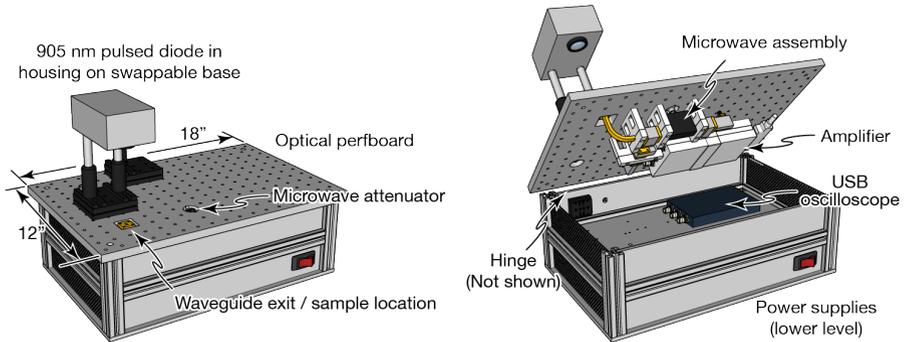
Figure 3.2. Time-resolved microwave photoconductivity spectrometer, utilized to measure lifetimes and surface recombination velocities of wafers.

3.3.2 Time-Resolved Microwave Photoconductivity Spectroscopy (TRMPS)

TRMPS measurements utilized an in-house-fabricated instrument where microwaves incident upon and reflected from a sample yields a detected power related to the dielectric function of the material. As charge carriers are generated under photodiode illumination the dielectric function is concomitantly altered yielding a change in the microwave reflectivity of the sample. Figure 3.2 presents a cartoon representation of the instrument, where the 25.4 mm hole pitch in the optical perfboard conveys the instrument scale. A Gunn oscillator generates Ka–band microwave radiation at 38.3 GHz that propagates via gold-plated WR28 waveguides through an attenuator to a microwave circulator after which the microwaves exit the $\sim 7 \times 2$ mm^2 waveguide for free-space propagation to an adjacent semiconductor sample. Reflected microwave power radiates back into the waveguide, through the circulator to a finline detector.

We adjusted the attenuator in the presence of a silicon sample but in the absence of illumination to yield $\sim$0.12 V at the detector. For photoinduced changes in conductivity, a $\sim$10 ns, 905 nm laser diode pulse generated charge carriers in the silicon wafer. The diode power was adjusted to generate $\sim 10^4$ photons per pulse as measured at a calibrated photodiode in its recommended, reverse-bias circuit (Thorlabs, FDS100-Cal) over a $\sim$0.05 cm^2 area. An oscilloscope recorded changes in microwave power the finline detector as a function of time, and a custom LabVIEW-based recorded >1000 acquisition averages. Following the acquisition, the LabVIEW-based program fit the acquired data to a single-exponential-decay function with both y-axis and x-axis offsets to yield the characteristic carrier recombination lifetime, τ. The lifetime is experimentally derived from this data, modeled by eq 3.1.

$$\frac{1}{\tau} = \frac{1}{\tau_{\text{B}}} + \frac{2S}{d} \qquad\qquad (3.1)$$

In eq 3.1, τ is the experimentally-measured lifetime, τ_{B} is the bulk recombination lifetime, d is the wafer thickness, and S is the surface recombination velocity.[5] We utilized $\tau_{\text{B}} = 242$ μs based on an experimentally-measured lifetime value for an i–Si wafer that was immersed in 1% ($\sim$ 0.5 M) HF$_{(aq)}$ and came from the same batch of wafers used for the silanization experiments.

3.3.3 Overlayer Model

The quantitative analysis for the visualization of the silane derivatized ultra-thin layered Nb_2O_5 silicon surface was computed by a Mathematica overlayer model adapted by Alexander D. Carl.[5] With this model, a relationship between silicon and niobium peak areas and organosilane fluorine peak areas was calculated in terms of nanometers on the surface. The conversion of the species signals is dependent on the attenuation lengths through pertinent materials. The silicon and niobium electrons are similar in energy so they are attenuated by the overlayer model by the same amount. These attenuation lengths are important for XPS overlayer analyses and therefore for certain species are well reported. For all XPS data, θ is 45°, this is the photoelectron collection angle as compared to the surface normal of the sample. From Abby D. Berube's thesis[18] the following equation below 3.2 for a three-layer model with fractional surface coverage is adapted for this project-specific surface species.

$$\frac{I_{\text{C}}}{I_{\text{A}}} = \frac{N_{\text{C}}\, SF_{\text{C}}}{N_{\text{A}}\, SF_{\text{A}}} \frac{\Phi_{\text{C}}\left(1 - \exp \frac{-d_{\text{C}}}{\lambda_{\text{C,self}} \cos\theta}\right)}{1 - \Phi_{\text{B}} + \zeta + \xi} \quad ...\text{where}... \qquad (3.2)$$

$$\zeta \equiv (\Phi_{\text{B}} - \Phi_{\text{C}}) \exp \frac{-d_{\text{B}}}{\lambda_{\text{A,B}} \cos\theta}$$

$$\xi \equiv \Phi_{\text{C}} \exp \frac{-d_{\text{C}}}{\lambda_{\text{A,C}} \cos\theta} \exp \frac{-d_{\text{B}}}{\lambda_{\text{A,B}} \cos\theta}$$

Equation 3.3 defines the relation between the photoelectron kinetic energy, E; the average atomic mass of the species in g mol^{-1}, $\langle A \rangle$; Avogadro's number, N; ρ, the overlayer density in kg m^{-3}; and finally, the average atomic number for atoms in the overlayer, $\langle Z \rangle$. [5]

$$\lambda = 0.316 \times 10^{12} \left(\frac{\langle A \rangle}{\rho N} \right)^{1/2} \left[\frac{E}{\langle Z \rangle^{0.45} \left(3 + \ln \frac{E}{27} \right)} + 4 \right] \tag{3.3}$$

Equation 3.4 was adapted from Alexander D. Carl's thesis[5] to calculate the intensity of the SiO_x interlayer atop the substrate Si(111) and under the Nb_2O_5 layer. Where ρ is the surface number density and D, is the unique thickness of the organic layer.

$$\frac{I_{Ox}}{I_{Si^0}} = \frac{\rho_{Ox}}{\rho_{Si^0}} \frac{\lambda_{Ox}}{\lambda_{Si^0}} \frac{1 - \exp \frac{-d_{Ox}}{\lambda_{Ox} \cos \theta}}{\exp \frac{-d_{Ox} - D}{\lambda_{Ox} \cos \theta}} \tag{3.4}$$

For an in-depth look into the calculations done by the overlayer model reference Appendix C for the complete derivations.

CHAPTER 4

RESULTS AND DISCUSSION

4.1 Results

A comparison of Si(111) surfaces in HF$_{(aq)}$ and H$_2$SO$_{4(aq)}$ was performed at the beginning of this project to have a lifetime reference for impending data. Fig. 4.2 shows this data, demonstrating how well i-Si performs in retaining photogenerated charge carriers with extremely low trap state densities. In HF$_{(aq)}$ i-Si has a lifetime of 1700 μs and a lifetime of 110 μs in H$_2$SO$_{4(aq)}$. From these experiments, the i-Si wafers were then left in air for multiple days and SRV was retaken, the resulting τ was 2 μs. This data will be further analyzed in the context of the primarily investigated tandem-junction system lifetimes later in Section 4.2.

XPS data collection was limited in the final months of the project due to unforeseen venting and water contamination in the UHV chamber. The XP spectra in Fig. 4.5 displays WPI–6 with Al$_2$O$_3$ and no organosilane surface derivatized. Once XPS is in optimal conditions again the study of WPI–6 (AlO$_x$) and WPI–4 (NbO$_x$) should be reinvestigated to verify the improved 10 mM silane recipe on ultra-thin NbO$_x$ versus thick layered AlO$_x$. This
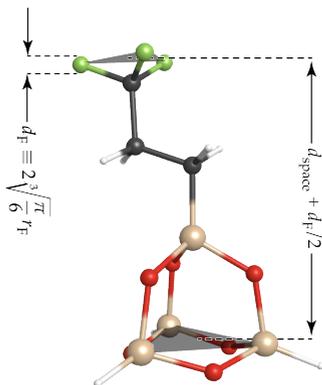
Figure 4.1. Ball and stick representation of the (3,3,3-trifluoropropyl)trimethoxysilane specifies how Abby Berude calculated the dimensions of the organosilane layer to the Nb_2O_5 interlayer.

is discussed further in Chapter 5. For WPI–6 and WPI–4 silane deposition was verified through the analysis of the water behavior on the surface of the samples and its apparent hydrophobicity.

WPI–8 and WPI–9 are the two most successful (3,3,3-trifluoropropyl)trimethoxysilane surface derivatization trials. Both were NbO_x deposited by Lehigh, sample 9 reacted with 10 mM of silane while 8 reacted with 2 mM. Fig. 4.5 shows regions Si 2p, Nb 3d, C 1s, O 1s, and F 1s. All regions are on the same scale respective to the species; therefore, photoelectron counts are relative to the peak areas.

The overlayer model for a 2 nm of Nb_2O_5 above 1.8 nm SiO_x that is consistent with our model for sample 8 demonstrates a Nb 3d : Si^0 2p = 6.78. The experimental Nb 3d : Si^0 2p ratio for sample 8 is 7.86, and the experimental ratio for sample 9 is 11.84. To see the specifics of these calculations reference C.

Beyond niobium and silicon ratios, the overlayer model for apical organosilane coverage included further spacing as defined in Fig. 4.1 for the distance between the fluorine atomic layer and the surface to which the silane is attached. AM1 calculations performed by Abby Berube demonstrated d_{space} = 0.698 nm. We further consider "square" fluorine as defined by $d_F = 2\sqrt[3]{\pi/6}\, r_F$ where r_F = 0.064 nm is the covalent radius of fluorine and d_F is the equivalently sized cube that is most relevant to linear depth models. The resulting model predicts a relationship between silane $–CF_3$ F 1s and substrate Si^0 2p ratios for systems in which silicon is successively covered by 1.8 nm of SiO_x, 2 nm Nb_2O_5, and 3,3,3-trifluoropropylsiloxy groups.
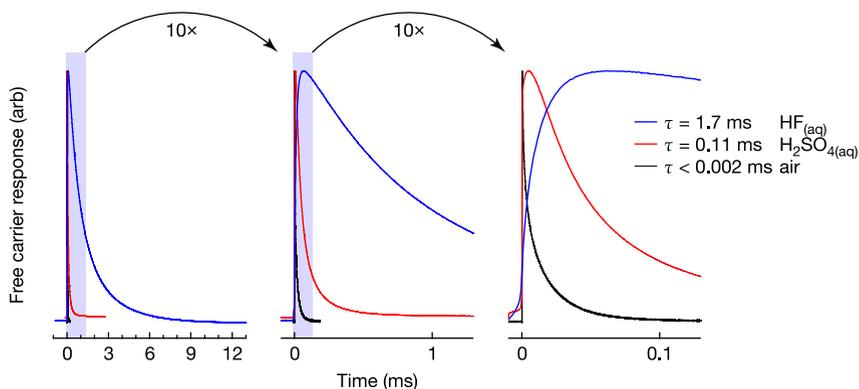
Figure 4.2. Side-by-side comparison of intrinsic silicon lifetimes in hydrofluoric acid, sulfuric acid, and in air. Used for reference to current ~1 ms for Al_2O_3 deposited samples and ~0.6 ms for Nb_2O_5 deposited samples. This is the future desired results for passivated and also solar applicable i-Si. Reinforcing the findings by Michalak et All [12]
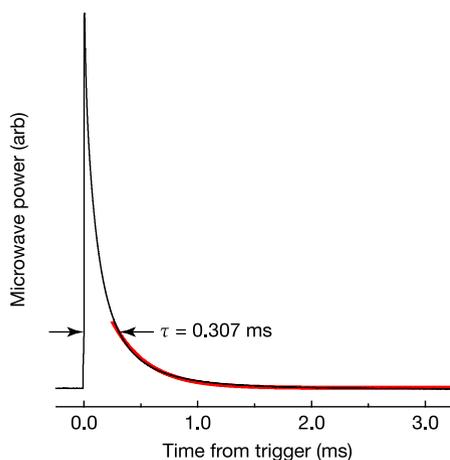
Figure 4.3. Exponential fit of sample WPI–9 demonstrating τ calculations per sample via TRMPS scans.

Fig.4.3 demonstrates how τ is calculated for each sample from the microwave photoconductivity spectra. The lifetime investigation was conducted before, following and for ~50 days after initial organosilane derivatization. Table 3.1 reports the initial SRV measurements from Lehigh after important experimental steps and our own initial SRV measurements after receiving the samples and one-month post aquirement. WPI–4's initial lifetime was 1036 μs which decreased to 985 μs after silanization. After ~50 days the final life-
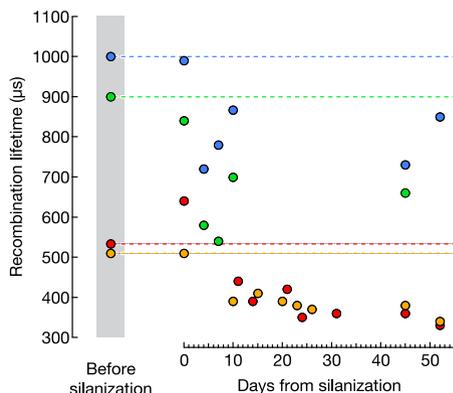
Figure 4.4. Lifetime values taken over ~50 days for samples WPI–4 (blue), 6 (green), 8 (orange) and 9 (red). Comparing before silane, immediately following silane, and the subsequent days.

time measurement was 852 μs resulting in an overall τ difference of 184 μs. WPI–6's initial lifetime was equal to 897 μs and then equal to 843 μs following silanization, the final τ measurement after 50 days was 590 μs. Resulting in an overall τ decrease of 307 μs. For WPI–8 the initial lifetime was 513 μs and 506 μs directly following silane derivatization. WPI–8 saw an overall change in the lifetime of 169 μs. And finally, WPI–9's initial τ was 533 μs and after silanization saw a sizable increase in surface lifetime to 639 μs. But after the 50-day study, the final lifetime did display a decrease of 200 μs. This data can be seen in Fig. 4.4

4.2   Discussion

The XPS results indicate successful deposition of (3,3,3trifluoropropyl)trimeth-oxysilane apical of the Nb_2O_5 layer. The XP spectra of WPI–6 with AL_2O_3 demonstrate how the thickness of the AlO_x layer prevents charge from passing through. The atomic layers of the Si substrate are infinitely thick compared to the metal oxide layer but their presence is nonexistent compared to the Si signal in the largest of the Nb peaks.

Trends vary when analyzing the lifetime data. Every sample experienced <100 μs decrease in lifetime after the initial functionalization of the surface with the organosilane, except for sample 9. This is promising for the next steps in the optimization of the silane recipe. Overall there is not enough XPS data to connect the quality of Nb to F contacts or Nb to Si contacts to the lifetime behavior. Recent studies imply that modeling long-chain organosilane derivatized surfaces based on fit XP spectra may require modification
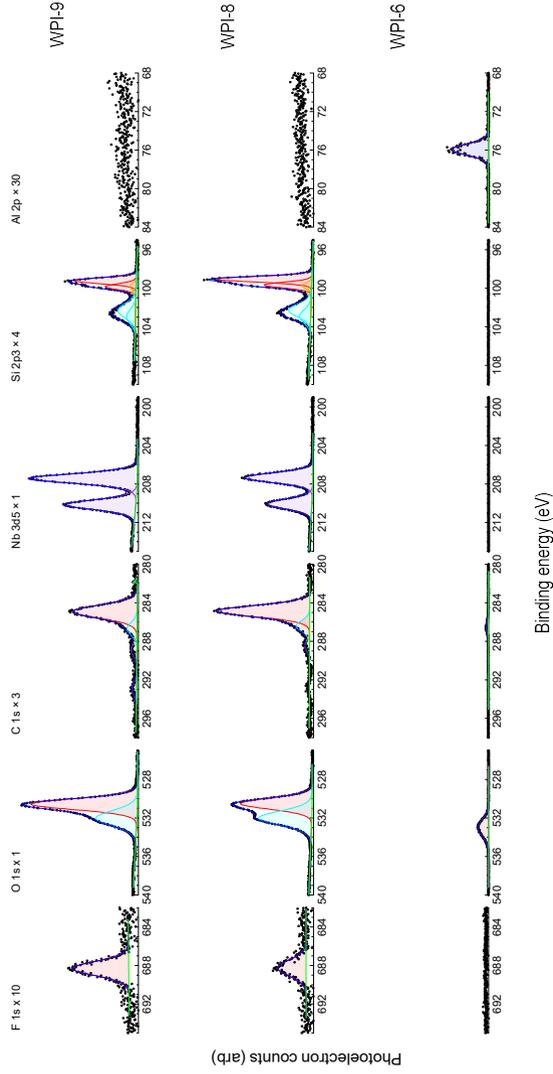
Figure 4.5. XPS data of samples WPI–6, 8, and 9. WPI–8 and 9 received Nb_2O_5 and silane and WPI–6 is only Al_2O_3. A comparison of Al_2O_3 and Nb_2O_5 thickness and silane chemical contacts.

due to unexpected attenuation from adventitious carbon.[19] It is promising to witness an initial increase to WPI–9′s τ after organosilane deposition and WPI–8′s minimal change in τ knowing that XPS verified the best Nb to F ratios of 0.494. These trends would benefit from further elucidation from the XP spectra of WPI–4 and WPI–6 with overlayer model analysis.

Beneficially low surface recombination velocities of intrinsic silicon in contact with strong acidic aqueous solutions are attributed to inversion or accumulation conditions despite the high density of trap states near the surface.[12] This phenomena is demonstrated in Fig. 4.2 The difference in lifetime of the Si(111) surfaces due to oxidation over 2–3 days is 1698 μs for HF$_{(aq)}$ contacts and 98 μs for H$_2$SO$_4$$_{(aq)}$ contacts. For the H$_2$SO$_4$$_{(aq)}$ etched sample the lifetime difference is comparable for the organosilane Nb$_2$O$_5$ deposited surface. Of more interest though is the HF$_{(aq)}$ etched samples that witness a 1698 μs decrease in 2–3 days after initial oxidation as compared to the ~200 μs over ~50 days for the investigated tandem-junction system. This is a promising result for the future of the effectiveness of Nb$_2$O$_5$ surface derivatized organosilanes on high-quality intrinsic silicon wafers.

CHAPTER 5

FUTURE WORK AND CONCLUSIONS

The data may not demonstrate the level of organosilane contact that we wanted to derivatize on the surface but it does show that deposition is possible and beneficial passivation can be observed as compared to ambient i-Si. Future areas of interest would be to optimize the silane recipe. 10 mM is possibly enough to create half a monolayer of silane with 10% surface coverage. Observing a complete monolayer of silane may produce trends of increased lifetime retainment among the samples. These data are calculated by an overlayer model that may or may not be accurate based on new studies of the impact that adventitious carbon has when long-chain hydrocarbon silanes are derivatized on Si surfaces.[19] Adjusting this overlayer model for the silane attenuation through carbon may result in an improved representation of the silane layer.

Developing the XPS verification of WPI–4, before and after silanization, and WPI–6, after silanization, would be conducive to a more complete analysis. A comparison of the effect of silane monolayers on top of Al_2O_3 may illuminate other crucial interactions that occur between the metal oxide surface and the Si. Which can be further utilized in specific studies of Nb_2O_5 in conjunction

with organosilanes. Also being able to compare these results again to ambient i-Si over the same time period will produce a more accurate picture of the impact that the pertinent deposited species have on the surface recombination velocities.

Future studies should also include atomic layer depositor commissioning experiments to improve in-house abilities to deposit the ultra-thin layers of Nb_2O_5. New Swagelok pneumatic valves and metal precursor cylinders will improve the quality of TMO layer linearity as it relates to the ALD cycles chosen. Further optimization of the ALD recipe may also improve instrument linearity and the overall quality of the TMO layers.

APPENDIX A

CESIUM TITANIUM BROMIDE (CS_2TIBR_6)

A.1 Experimental

Usual procedures for Cs_2TiBr_6 synthesis focused on large-grain crystals but this appendix will detail improved procedures that focus on the synthesis of thin-film Cs_2TiBr_6 on FTO Glass and silicon wafers.

A.1.1 Thin Film on FTO and Silicon Substrates

Original experiments were completed on fluorine-doped tin oxide (FTO) glass which consisted of one side of the glass and one side of charged FTO films. First, the FTO glass substrate was tested with a voltmeter to verify which side was charged and which was not. It was then cut into four pieces and scribed on the non-charged side for easier identification of the individual samples. They were cleaned by placing the samples and acetone in a test tube and sonicated for about five minutes. This process would then be repeated with isopropyl alcohol (IPA) and water. FTO Samples were then left in the

Table A.1. Heating recipe for Cs$_2$TiBr$_6$ as inserted into LabVIEW program for the Neptune furnace.

Furnace Action	Front Temp (°C)	Back Temp (°C)	Time (h)
Ramp to	200	215	6
Go/hold at	200	215	18
Ramp to	180	200	5
Ramp to	70	40	1
Ramp to	0	0	0

lab oven for about thirty minutes to completely dry and then brought back to the bench. Silicon samples were also cut at the glass cutting bench along its specific crystalline axis. Single-sided n$^+$ or double-sided p$^+$ Si(111) were used as received and were doped with arsenic and boron, respectively. Four pieces were cut and sonicated in the same manner as the FTO films.

After they are clean the samples were placed on the spin coater so that an aqueous solution of 1.5 M CsBr (Pure, 99.9%, Acros Organics) and a 50/50 solution of water and ethylene glycol could be uniformly deposited on the surface. Each individual sample received about 1 mL of precursor via a syringe and spun for one minute with a speed of 1500 rotations per minute(rpm) accelerating at 150–200 rpm s^{-1}. Each spin deposition was completed with laminar N$_2$ gas flowing on the surface to improve film uniformity. Once a thin film of CsBr was deposited the samples would be dried on a hot plate at 125 °C for ~20 min.

Once the CsBr was successfully deposited the next step was to react the samples with the final reactant TiBr$_4$. Two samples, a glass reaction vessel, a gasket, and a cap were then pumped into the lab's glovebox. TiBr$_4$ must be kept under constant nitrogen flow or the titanium will oxidize, destroying the compound and causing toxic vapors to enter the air. Between 200 mg and 180 mg were measured out of the sublimated TiBr$_4$ stock and added to the reaction vessel with the samples. The gasket and cap were then utilized to close the reaction vessel so that it is airtight. The system was transferred to the lab's Neptune furnace and underwent the heating recipe in Table A.1.

A.1.2 Atomic Layer Deposition (ALD)

Cesium Titanium Bromide (Cs$_2$TiBr$_6$) is extremely air sensitive. The titanium atoms instantly react with the oxygen from the atmosphere to create titanium dioxide (TiO$_2$) and the cesium bromide (CsBr) that is left becomes amorphous and liquid-like. In an attempt to passivate the surface from oxidation, the metal precursor TiO$_2$ was chosen to be atomically layered on the surface. TiO$_2$

is not only created during the atmospheric decomposition of Cs_2TiBr_6 but it also has complementary band gap values. This makes it a good candidate for surface passivation on both substrates.

Once the thin film Cs_2TiBr_6 was deposited on the surface of the FTO glass or silicon wafer and verified by XRD, the samples were brought back into the glovebox where they were loaded into the main reaction tube of the ALD reactor. The glass elbows on either side of the reaction tube were secured with Dow Corning vacuum grease and keck clamps. The stopcocks would also be greased and closed shut to prevent any air from leaking into the system. It was then brought over to the ALD and attached to the rest of the Schlenk line. The ALD was slowly pumped down, the big pump trap and smaller reactor trap were cooled with liquid nitrogen. Once the pressure gauge read below 20 torrs the recipe was entered and queued in LabVIEW and the reaction was run. Below is the table of the micro pulses, temperatures, and other parameters pertinent to the Cs_2TiBr_6 thin-film passivation.

After the ALD was run the system were closed off and transferred to the glovebox where it would be disassembled and loaded for characterization and analysis. The atomic layer depositor features and progress are further detailed in Appendix B.

A.2 Data Collection

A.2.1 X-ray Diffraction (XRD)

X-ray diffraction (XRD) was used to verify the presence of cesium titanium bromide (Cs_2TiBr_6) on the surface of either substrate. The sample, an XRD plate, and Kapton tape were pumped into the glove box. Two pieces of Kapton tape were needed to prevent the destruction of the sample during XRD analysis. One piece was taped to the sticky underside of the other so that when the sample was taped over, it would not adhere to the Cs_2TiBr_6 thin film. Air-tight sealing on all sides was verified before its removal from the glove box.

It was then transferred to the XRD where it was loaded and Diffrac plus XRD Commander is booted up and the scanning parameters are entered. The energy is set to 40 kV and 40 mA, 0.1 increments, 20 sec/step and the scan is run through the range 27–31.5°. The Kapton tape caused a shift in the peaks as compared to their original positioning but the overall area and peak identification is detailed later in §A.3.

A.2.2 X-ray Photoelectron Spectroscopy (XPS)

After XRD verification the sample was transferred back to the glove box, along with an IPA-cleaned X-ray photoelectron spectroscopy (XPS) puck,

Figure A.1. Qualitive representation of what good product yield looks like for Cs_2TiBr_6 thin-films deposited on FTO glass.

carbon tape, copper tabs, and screws. If the substrate of the sample was FTO glass, carbon tape was used to load the sample onto the XPS puck, otherwise, copper tabs and screws were used to hold the silicon samples in place. After the sample is successfully loaded onto the XPS puck, an air-free steel vacuum suitcase was used to transfer the sample from the glove box to the XPS. The load lock was first opened to the XPS's rough pump where it was left to equilibrate until the gauge read below 250 mTorr. From there it was closed off from the rough pump and opened to the turbo pump where it was pumped on for another hour. The vacuum suitcase was then aligned precisely with the opening of the main load lock, this was done to avoid having to expose the sample to air so that it may be attached to the fork. Once attached, the suitcase and load lock was evacuated together and the arm was brought down so that the fork could come forward and grab the puck. From there, the vacuum suitcase arm would detach and be retracted. The load lock was isolated from the suitcase and pumped on again by both pumps so that the pressures of the main chamber and antechamber were $<10^{-9}$ Torr. The door connecting the load lock and main chamber was lifted and the puck was transferred from the fork to the stage. The fork was retracted and the door sealed.

The next step was to use AugerScan program to align the stage and sample with the incident X-rays. The multiplex and survey scans were loaded into the automation window, and regions of cesium, titanium, bromine, carbon, oxygen, and nitrogen were scanned to verify not only the presence but also chemical bonding and contamination. These scans were then fit in the XPS peak fitting program for numerical analyses. This analysis was performed thoroughly by Jocelyn Mendes in her senior thesis. [20,21]

A.3 Qualitative Results

Majority of the analysis executed on Cs_2TiBr_6 were XRD. XPS was attempted but transferring between the glove box and XPS usually resulted in exposure that destroyed the films created. Figure A.1 presents a qualitative example of what decent Cs_2TiBr_6 thin films will look like immediately out of the reactor furnace before being cracked in the glove box. The red-orange tint is the
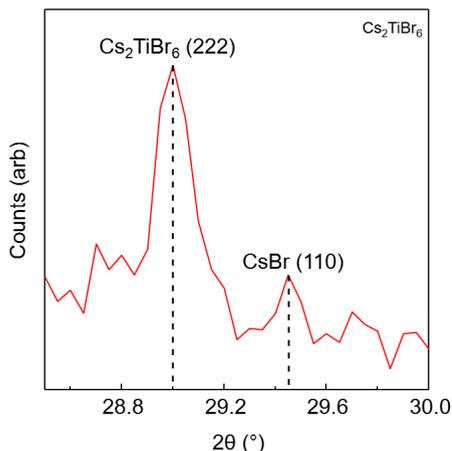
Figure A.2. XRD data showing relative peaks of product Cs_2TiBr_6 (28.9°) compared to reactant CsBr (29.4–29.6°)

signature color of Cs_2TiBr_6 which is a deep maroon red in its large-grain crystalline form. While these films show satisfactory product formation on the surface the uniformity of deposition should be verified with further XPS investigations.

Figure A.2 depicts the X-ray diffraction caused by crystalline product Cs_2TiBr_6 and one of the reactants CsBr. Showing relative presence on the surface of the FTO glass. Cs_2TiBr_6 has a characteristic peak at ~28.9°. CsBr has a characteristic peak at ~29.6°. These peaks may be displaced depending on the technique used to scan in the XRD. The XRD is utilized in air and that will destroy the sample before measurements can be taken. Here a cover of Kapton tape was used to keep oxidation from occuring, which is a destructive process when the Kapton tape is removed. Later data collection was one step in a long process of characterizing the films and also passivating them, therefore a double layer of Kapton tape would be utilized to keep the films from being removed in the process which caused a displacement of the characteristic peaks in the XRD data.

APPENDIX B

ATOMIC LAYER DEPOSITON (ALD)

The in-house-built, Schlenk-line-incorporating, atomic-layer-deposition ALD instrument contains *all* of the compound adjectives. Further, it was first assembled by undergraduate Jocelyn Mendes, and Dr. Julia Martin. This appendix section will label all progress and adjustments that have occurred since its original construction. It also provides information about the forming gas annealing furnace, its assembly, and directions for use.

B.1   Instrument Set-Up

The in-house built Schlenk line adapted ALD was the main instrument employed to react the niobium precursor with the surface of the cleaned silicon wafers and Cs_2TiBr_6 thin-films (detailed in Appendix A). The ALD consists of an electronics board set-up encased in polycarbonate within the fume hood that connects the manifold, reactor, and precursors to the computer with Lab-VIEW and other relevant programs. Additionally, it consists of the manifold

Figure B.1. Atomic layer depositor with metal precursors, electronics board, schlenk-line inside the lab fume hood.

and reactor portion that carries out the physical reaction, which is located in the fume hood. The ALD was used for many air-free experiments so the Schlenk line was constantly being pumped on by an oil diffusion pump that kept it below 1×10^{-3} Torr. The Mass Flow Controller (MFC) (Aera FC-770AC) allowed for control of the inert carrier gas, nitrogen (N_2), that was used. All of which can be viewed in figureB.1 above.

B.1.1   Electronics

The electronics within the fume hood board are composed of 2 barrier strips (WM5766-ND, Digi-Key), a TC Gauge 120 VAC receptacle (Q337-ND, Digi-Key), solenoid connections, a multifunction I/O device (NI USB 6216, National Instruments), several power supplies, and a circuit breaker switch. The initial barrier strip connects to the Mass Flow Controller (MFC) to dictate power and signal, along with the four pneumatic valves. The TC Gauge 120 VAC receptacle powered the five temperature controllers (LOVE 32B, Dwyer Instruments, Michigan City, IN) and heated the ALD furnace along with one of the gauges being used to measure the pressure within the Schlenk line. Next, the multifunction I/O device connected to a USB Hub (BYEASY

USB 2.0 Hub 7 Ports, Amazon) connected the electronics to the computer for communication. The power supplies are specified as +5 V and +24 V, which powered the USB hub and the solenoid connections, and the other ±15 V power the 2 barrier strips. Finally, the 15A circuit breaker switch allowed for quick and easy disabling and enabling of the whole board.

B.1.2   Reactor and Precursors

The main components of the reactor are the center quartz (15 in 24/40 ₮) or Boron tubing connected to an in-house-crafted left and right elbow piece (also 24/40 ₮).   The fittings were secured by a high-temperature vacuum grease (Dow Corning) that enabled an airtight seal. The left elbow connected the reactor to the down tube which the precursors traveled through before surface depositing. It was important that the elbow was kept at least at the same temperature as the precursor to prevent premature deposition, so electrical heat tape, fiber quartz, and aluminum layers were used to wrap the elbow up until it connected with the reactor. The right elbow attached the reactor to a liquid Nitrogen cooled trap, which collected any excess reactants and prevented them from traveling back up into the Schlenk line. The Schlenk line connected the ALD apparatus to the pump which allowed for it to be kept under vacuum during experiments. It also allowed for the ALD to be pumped with an argon backflow when experiments were finished, aiding in safely depressuring the system. The Schlenk line had four stopcocks which were sealed with the same high-temperature vacuum grease: two were connected to atmospheric air, one connected to the ALD chamber and the last one opened to the argon flow.

Up the down tube, the three precursors were held in their respective containers labeled D1, D2, and D3. The first was the water precursor, the second was a titanium precursor, tetrakis(ethylmethylamino)titanium (TiO_2, 99%, Strem Chemicals Inc.), and finally the niobium precursor, (*tert*-butylimido)-*tris*(diethylamino)-niobium (TBTDEN, $(CH_3)_3CNNb(N(C_2H_5)_2)_3$). The setup for each was the same, a VCR face seal fitting connected to a male VCR fitting and a male NPT body connector and fitting that attaches to a two-way pneumatic Swagelok valve (SS-4-VCR-1-4, Swagelok). The NPT pipe is the main body portion which was closed with a female NPT cap. Each was filled with 10–20 mL of their respective reactant, which left enough room in the headspace for a collection of vapors to be released when the pneumatic valves were activated.

B.2   Annealing Furnace Construction

The apparatus utilized for annealing seen in Fig. B.2 was an in-house furnace with a heating recipe dictated by an input on the LabVIEW program as seen in Table B.3. This furnace held a special 72cm quartz tube connected on one side

Figure B.2. Forming gas apparatus constructed for the realignment of Nb_2O_5 ultra-thin layers on the wafers surface. The pictured state does not have the plastic tubing running through the oil bubbler.

to a forming gas (5/95% H2/N2) tank and on the other an oil bubbler. The tube was switched out when annealing different species to avoid contamination. A stainless steel tube adapter in conjunction with a Balzer's connector and a Swagelok 316 X US fitting connected a plastic gas line from the forming gas tank to the quartz reactor tube. The tank had a Harris Model 425 · 125A regulator with a Generant Y54-1 valve for finer flow control. The gas flow was adjusted based on the bubbling that occurred in an oil bubbler, which was observed and adjusted throughout the trials, connected to the quartz via the same fittings.

B.3   Experimental

The n-dopant and p-dopant silicon wafers were used throughout the project to optimize the ALD recipe. Prepping, loading, and unloading the ALD was

Table B.1. ALD heated segments and the segment's maintained temperatures.[a]

ALD Segment	Temperature (°C)
Manifold 1	140
Water Precursor	50
D2 Metal Precursor	115
Down Tube	160
ALD Furnace	150
D3 Metal Precursor	110

[a] These are consistent at all times except for the reactor, when a program is not running the reactor is switched to 0°C.

consistent for each wafer. The sample was chosen, recorded, and dried with an argon gas gun connected to an argon tank. The wafer was loaded into the quartz tubing inside the reactor and shifted with an IPA clean scapula to avoid contamination, optimal gas flow occurs across the side of the wafer faced upward and on SSP n$^+$-Si the polished side has to be face up. The right arm was not attached at this point and all connections to the Schlenk line from the ALD were closed to prevent depressurization. Once the sample was properly loaded the thermocouple was checked to make sure it was reading accurately. The right elbow was dabbed with vacuum grease and a stable seal was established between the reactor tube and the glass elbow. Silicon tubing was used to connect the right elbow with the trap then tightened with copper wiring. The trap was secured with a Breeze stainless steel PVC pipe tightener, back to the ALD. Once the system was verified to be isolated, each valve was opened slowly starting at the down tube, next, the reactor tube, then the trap, and finally by closing the valve between the trap and the down tube. Each valve will cause a pressure spike, waiting until the pressure has bottomed out will allow the least amount of air to be introduced to the sample. If the connections were secure the reactor was then closed, and any gaps were filled with fiber quartz to encourage temperature uniformity. The niobium and water precursors were double-checked to make sure they were open to the down tube and the traps were filled with liquid nitrogen and covered with fiber quartz and aluminum foil. The ALD was then considered to be in the run position and ready to run an experiment.

The next step was inputting the recipe into the LabVIEW program to run. The ALD recipe was comprised of three major parameters: the temperatures seen in Table B.1, the micropulse settings in Table B.2, and the cycle settings in Fig. B.3. The precursor and furnace temperatures were altered to increase deposition but once decided on, did not change.

1: ☑Set ALD running temperatures defined in temp program?

2: Initial wait time 30 minutes (>0 numbers are changable during run!)

3: MFC Run SP 5 sccm (changable up until execution)

4: More waiting 15 minutes (>0 numbers are changable during run!)

5: Cycle 10 time(s)... (this number is changable during an ALD run!)

Pulse D1 ⌄ then wait 5 sec (fixed during run)
then pulse D3 ⌄ then wait 60 sec (fixed during run)
☐then pulse D1 ⌄ then wait 5 sec (fixed during run)

6: ☑ Finish with pulse D1 ⌄ then wait 5 seconds

7: ☑Set ALD standby temperatures defined in temp program?

8: MFC Stdby SP 0 sccm (changable up until execution)

Figure B.3. The LabVIEW recipe of cycle parameters and metal precursor settings. Only shows up to step 8 but step 9 contains contact information to alert users when the cycle is complete. Once filled hit "Go recipe!"

Table B.2. The micropulse settings of the ALD during the Nb_2O_5 experiments.

Metal Precursor	# of Pulses	Time (ms)	Micropulse Time (ms)
Nb_2O_5	2	20	980
H_2O	1	20	1980

Table B.3. Forming gas annealing recipe as outlined in the furnaces' LabVIEW program.

Furnace Action	Front Temp (°C)	Back Temp (°C)	Time (h)
Ramp to	350	350	1
Soak at	350	350	1
Ramp to	0	0	1

After the run was finished the wafer was unloaded and the ALD was returned to the idle position. The first step was to allow the reactor to cool so that it may be handled safely, so the fiber quartz is removed and the reactor is left open while the Schlenk line is backfilled with Argon gas. The down tube was isolated and the line connecting the trap to the down tube was opened. After that, the small right-side trap was dropped and the stopcock connecting the ALD to the rest of the Schlenk line was closed off. The argon flow was established by observing an oil bubbler. Once the flow was set, the stopcock connecting to the ALD was turned to the argon line and left open to it for 30–60 seconds. The argon flow was then cut, and the stopcock was closed again to both lines. The ALD was then at passive atmosphere and could be opened to air without resistance, it was opened by the rubber tubing behind the small trap to help minimize the mishandling of fragile glassware. Once everything was cooled to room temperature, the far-right elbow was detached and cleanly stored for the next run. The big trap was also replaced to prevent reactants from traveling to the pump. The ALD was then pumped down again and left in this idle position for loading when ready. The sample was removed and ready for the next step of annealing.

The next step is annealing via the annealing furnace. The side closest to the entrance of the hood was utilized for access into the quartz tube of the annealing furnace. The samples were placed inside the tube and again position properly with a long scapula. The fittings of the tube were replaced and secured and then fiber quartz was utilized to maintain the temperature gradient within the furnace. Once in place, the regulator and finer gas flow valves were opened and adjusted for optimal gas flow by the observance of the oil bubbler. The recipe, shown here in Table B.3 was entered into

the LabVIEW program and ran. Throughout experimentation, the flow was adjusted down during the temperature ramp-ups and increased during the temperature ramp-downs.

APPENDIX C

MATHTHEMATICA CALCULATIONS

The following pages detail the adaptation of Abby Berube and Antonio Ramirez's overlayer models in *Mathematica* to best describe the silanization of niobium-oxide-coated Si(111).

In[1]:= (* A Pellerin which occurred...*)

(* A Mathematica notebook for something
 Updated 24 April 2023 -- ejp *)

In[2]:= Avogadro = 6.022 × 10²³;

In[3]:= (* OmniFocus III analyzer
  angle vs surf normal *)

$$\Theta = \frac{\pi}{4};$$

In[4]:= (* Sensitivity factors for Phi
   5600 instrument with OmniFocus III
   analyzer and mono illumination *)

SFF = 1.000;

SFSi = 0.283;

SFNb = 2.517;

In[7]:= SiUnitCellLength = 0.543090;

(* Units are nanometers *)

In[8]:= $\text{Sibondlength} = \dfrac{\text{SiUnitCellLength}}{\sqrt{2}};$

In[9]:= $\sigma\text{Si111} = \dfrac{2 \times 2}{\sqrt{3}\ \text{SiUnitCellLength}^2}$

(* surface packing density in nm⁻²*);

In[10]:= $\rho\text{Si} = \dfrac{8}{\text{SiUnitCellLength}^3}$

(* Units are atoms nm⁻³ *);

In[11]:= (*Let's say that silanes can cover 70
   % of the density of Si(111) sites...*)

In[12]:= σSilane = 0.3 $\times$ σSi111

Out[12]= 2.34897

In[13]:= (* Niobium unit cells lengths in nanometers*)
aNb = 0.3872;
bNb = 1.9789;
cNb = 2.0814;
NbUnitCellVolume = aNb $*$ bNb $*$ cNb;

In[17]:= (* Density of niobium atoms in Nb2O5*)

$$\rho\text{Nb} = \frac{28}{\text{NbUnitCellVolume}^3}$$

(* Units are atoms nm^{-3} *)

Out[17]= 6.90262

In[18]:= (* Thickness of fluorine layer based on
covalent F atomic radius via H.B. Gray,
ISBN 978-0935702354 *)

$$\text{dF} = \sqrt[3]{\frac{\pi}{6}} \times 2 \times 0.064$$

Out[18]= 0.103167

In[19]:= $$\rho\text{F} = \frac{\sigma\text{Silane} \times 3}{\text{dF}};$$

(* Three fluorines per silane *)

In[20]:= (* Spacers... estimate F distance
    in between the niobium oxide surface
    and the F layer. Importantly,
  this does not include either the niobium
      oxide or the F themselves! If we had a
      distance for F - UiO cluster distance,
  we could subtract FThick/2 to get this
    number. ABBY BERUBE ran an AM1
    calculation on a trifluoropropyl
    silane attached to a siloxane cluster
    to enforce normal alignment of the Si-
  C in the silane to the surface...
    see Figure 3.2.X in ADBThesis! *)
  dFtoNbOx = 0.698 - $\frac{dF}{2}$;

In[21]:= (* Attenuation lengths in nm*)
  λF = 2.05;
  (* Attenuation approximation length of F from
    10.1016/j.polymer.2003.08.038 in nm *)

  λSiself = 2; (* Attenuation length
    of Si2p through bulk silicon *)
  λSiOxself = 3.485; (* Attenuation length
    of Si2p through silicon oxide *)
  λNblit = 5.8; (* Attenuation length of
      Nb3d through Nb2O5 itself from https://
    accelconf.web.cern.ch/SRF97/papers/
      srf97d18.pdf *)
  NbAvgAtomicNumber = $\frac{41 \times 2 + 8 \times 5}{7}$;

In[26]:= `NbAvgMolarMass` $= \dfrac{92.90637 \times 2 + 15.9994 \times 5}{7}$;

In[27]:= `Nb2O5density = 4550 ;` $(*$ `kg m`$^{-3}$ $*)$

`λNbcalc =`

$$0.316 * 10^{12} \left(\frac{\texttt{NbAvgMolarMass}}{\texttt{Nb2O5density} * 6.02 * 10^{23}} \right)^{1/2}$$

$$\left(\frac{1486 - 202}{\texttt{NbAvgAtomicNumber}^{0.45} * \left(3 + \texttt{Log}\left[\frac{1486 - 202}{27} \right] \right)} + 4 \right)$$

Out[28]= `2.07268`

In[29]:= `λNb = λNbcalc;`

In[30]:= `λSiNbcalc =`

$$.316 * 10^{12} \left(\frac{92.9}{\texttt{Nb2O5density} * 6.02 * 10^{23}} \right)^{1/2}$$

$$\left(\frac{1486 - 99}{14^{0.45} * \left(3 + \texttt{Log}\left[\frac{1486 - 99}{27} \right] \right)} + 4 \right)$$

$(*$ `Si 2p electrons going through Nb2O5` $*)$

Out[30]= `3.78017`

In[31]:= `λSiNb = λSiNbcalc`

Out[31]= `3.78017`

In[32]:= `ORGANICaveZ` $= \dfrac{3 \times 6 + 4 \times 1 + 3 \times 8 + 1 \times 14 + 3 \times 9}{3 + 4 + 3 + 1 + 3}$;

$(*$ `Average atomic number of the atoms`

`in organic layer assuming` $C_3O_3H_4Si$ $*)$

In[26]:= $\text{NbAvgMolarMass} = \dfrac{92.90637 \times 2 + 15.9994 \times 5}{7}$;

In[27]:= $\text{Nb2O5density} = 4550$; (* kg m^{-3}*)

$\lambda\text{Nbcalc} =$

$0.316 * 10^{12} \left(\dfrac{\text{NbAvgMolarMass}}{\text{Nb2O5density} * 6.02 * 10^{23}} \right)^{1/2}$

$\left(\dfrac{1486 - 202}{\text{NbAvgAtomicNumber}^{0.45} * \left(3 + \text{Log}\left[\frac{1486 - 202}{27} \right] \right)} + 4 \right)$

Out[28]= 2.07268

In[29]:= $\lambda\text{Nb} = \lambda\text{Nbcalc}$;

In[30]:= $\lambda\text{SiNbcalc} =$

$.316 * 10^{12} \left(\dfrac{92.9}{\text{Nb2O5density} * 6.02 * 10^{23}} \right)^{1/2}$

$\left(\dfrac{1486 - 99}{14^{0.45} * \left(3 + \text{Log}\left[\frac{1486 - 99}{27} \right] \right)} + 4 \right)$

(* Si 2p electrons going through Nb2O5 *)

Out[30]= 3.78017

In[31]:= $\lambda\text{SiNb} = \lambda\text{SiNbcalc}$

Out[31]= 3.78017

In[32]:= $\text{ORGANICaveZ} = \dfrac{3 \times 6 + 4 \times 1 + 3 \times 8 + 1 \times 14 + 3 \times 9}{3 + 4 + 3 + 1 + 3}$;

(* Average atomic number of the atoms
in organic layer assuming $C_3O_3H_4Si$*)

In[33]:= ρORGANIC = 1500;

(*Assuming $C_3O_3H_4Si$ the mass would be 116.15
    g/mol and is in volume of FtoZrspace so...
  making up an average between 2.2 PTFE
  10.1007/s10765-008-0512-z and .9 HDPE
  10.1016/j.compscitech.2007.04.024*)

ORGANICaveformulamass =
  $\left(12.01 \times 3 + 4 \times 1 + 3 \times 16 + 28 + 19 \times 3\right) /$
    $\left(3 + 4 + 3 + 1 + 3\right)$;

(* Average formula mass from Zr-O bonds to
  top carbon which makes up organic layer*)

(*Attenuation values for zirconium through
 the organic layer and through itself*)

In[35]:= KENb3d = 1486 - 207;

In[36]:= λNbthroughorganic =
    $0.316 \times 10^{12} \times \left(\dfrac{\text{ORGANICaveformulamass}}{\rho\text{ORGANIC} \times \text{Avogadro}}\right)^{1/2} \times$

    $\left(\dfrac{\text{KENb3d}}{\text{ORGANICaveZ}^{0.45} \times \left(3 + \text{Log}\left[\frac{\text{KENb3d}}{27}\right]\right)} + 4\right)$

Out[36]= 3.17766

In[37]:= KESi2p = 1486 - 99

Out[37]= 1387

In[38]:= λSithroughorganic =

$$0.316 \times 10^{12} \times \left(\frac{\text{ORGANICaveformulamass}}{\rho\text{ORGANIC} \times \text{Avogadro}} \right)^{1/2} \times$$

$$\left(\frac{\text{KESi2p}}{\text{ORGANICaveZ}^{0.45} \times \left(3 + \text{Log}\left[\frac{\text{KESi2p}}{27} \right] \right)} + 4 \right)$$

Out[38]= 3.39511

In[39]:= ExperimentalOxIntensityRatio =
0.782 (* from ejp data for WPI 8
post silane PUT IN DATE SCANNED!! *)

Out[39]= 0.782

In[40]:= OxideThickness[experimentalratio_] :=
2.464 * Log$\left[(1.41 * (\text{experimentalratio})) + 1 \right]$
(* experimental ratio obtained from XPS,
Iox/Isi *)
OxideThickness[ExperimentalOxIntensityRatio]
(* cite alex's first paper
in ACS Appl. Mater. Interfaces *)

Out[41]= 1.83121

In[42]:= NiobiumIntensity[d_] :=
$$\rho\text{Nb} * \text{SFNb} * \left(1 - \text{Exp}\left[\frac{-(d)}{\lambda\text{Nb} * \text{Cos}[\theta]} \right] \right) *$$

$$\left(\text{Exp}\left[\frac{-\text{dFtoNbOx} - \frac{\text{dF}}{2}}{\lambda\text{Nbthroughorganic} * \text{Cos}[\theta]} \right] \right)$$

In[46]:= `Plot[NiobiumIntensity[x] / SiliconIntensity[x,`
`ExperimentalOxIntensityRatio], {x, -0.1, 5}]`

Out[46]=
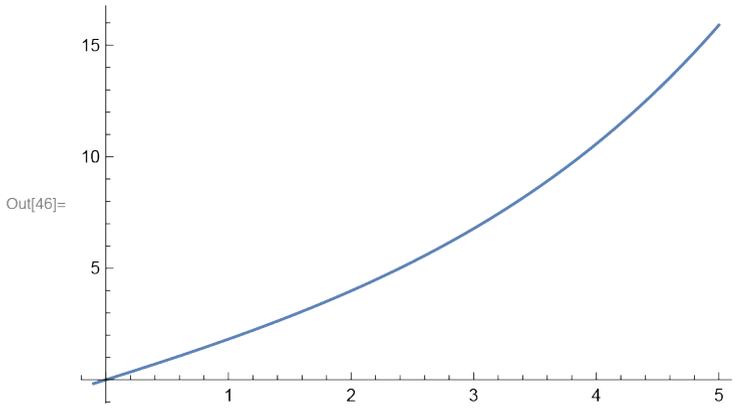
In[47]:= $$\frac{NiobiumIntensity[2]}{SiliconIntensity[2, OxideThickness[0.78]]}$$

Out[47]= `6.78147`

In[48]:= $$\frac{FluorineIntensity}{NiobiumIntensity[2]}$$

Out[48]= `0.494917`

In[49]:= $$\frac{FluorineIntensity}{SiliconIntensity[2, OxideThickness[0.78]]}$$

Out[49]= `3.35626`

APPENDIX D

REFERENCES

1. Hannah Ritchie, M. R., and Pablo Rosado. CO_2 and Greenhouse Gas Emissions. 2020. (accessed 2022-10-15).

2. Kumar, A.; Nagar, S.; Anand, S. 1 - Climate change and existential threats. In Global Climate Change, Singh, S., Singh, P., Rangabhashiyam, S., Srivastava, K. K. Eds.; Elsevier, **2021**; pp 1–31.

3. Holly Shaftel, S. C., Randal Jackson, and Daniel Bailey. How Do We Know Climate Change Is Real? NASA, 2023.
https://climate.nasa.gov/evidence/ (accessed 2023).

4. Velicogna, I.; Mohajerani, Y.; A, G.; Landerer, F.; Mouginot, J.; Noel, B.; Rignot, E.; Sutterley, T.; Van Den Broeke, M.; Van Wessem, M.; et al. Continuity of Ice Sheet Mass Loss in Greenland and Antarctica From the GRACE and GRACE Follow-On Missions. *Geophys. Res. Lett.* **2020**, *47* (8), e2020GL087291.DOI: 10.1029/2020gl087291.

5. Carl, A. D.; Grimm, R. L. Covalent Attachment and Characterization of Perylene Monolayers on Si(111) and TiO$_2$ for Electron-Selective Carrier Transport. Langmuir **2019**, *35* (29), 9352–9363. DOI: 10.1021/acs.langmuir.9b00739.

6. History of Photovoltaics. Florida Solar Energy Center, 2014. history_of_pv.htm (accessed 2023).

7. Solar Energy. SESCI, (accessed 2023).

8. Hayat, M. B.; Ali, D.; Monyake, K. C.; Alagha, L.; Ahmed, N. Solar energy-A look into power generation, challenges, and a solar-powered future. *Int. J. Energy Res.* **2019**, *43* (3), 1049–1067. DOI: 10.1002/er.4252.

9. Ramirez, Antonio. Deposition of Ultrathin Films of Niobium Pentoxide onto n$^+$-Si(111) Using Atomic Layer Deposition. Worcester Polytechnic Institute, **2022**.

10. Leach, C. J.; Davis, B. E.; Garland, B. M.; Thorpe, R.; Strandwitz, N. C. Ultrathin atomic layer deposited niobium oxide as a passivation layer in silicon based photovoltaics. *J. Appl. Phys.* **2021**, *130* (21), 215301. DOI: 10.1063/5.0067281 (acccessed 4/21/2023).

11. Gleason-Rohrer, D. C.; Brunschwig, B. S.; Lewis, N. S. Measurement of the Band Bending and Surface Dipole at Chemically Functionalized Si(111)/Vacuum Interfaces. *J. Phys. Chem. C* **2013**, *117* (35), 18031–18042. DOI: 10.1021/jp401585s.

12. Michalak, D. J.; Gstrein, F.; Lewis, N. S. Interfacial Energetics of Silicon in Contact with 11 M NH4F(aq), Buffered HF(aq), 27 M HF(aq), and 18 M H2SO4. *J. Phys. Chem. C* **2007**, *111* (44), 16516–16532. DOI: 10.1021/jp074971d.

13. Yu, G.; Liu, C.; Gao, H.; Wang, T.; Wu, X.; Lin, P.; Xu, L.; Cui, C.; Yu, X.; Wang, P. Activation and Deactivation of Silicon Surface Passivation by Niobium Oxide Films. *Phys. Status Solidi RRL* **2022**, *16* (6), 2100649. DOI: 10.1002/pssr.202100649.

14. Michalak, D. J.; Gstrein, F.; Lewis, N. S. The Role of Band Bending in Affecting the Surface Recombination Velocities for Si(111) in Contact with Aqueous Acidic Electrolytes. *J. Phys. Chem. C* **2008**, *112* (15), 5911–5921. DOI: 10.1021/jp075354s.

15. Gstrein, F.; Michalak, D. J.; Royea, W. J.; Lewis, N. S. Effects of Interfacial Energetics on the Effective Surface Recombination Velocity of Si/Liquid Contacts. *J. Phys. Chem. C* **2002**, *106* (11), 2950–2961. DOI: 10.1021/jp012997d.

16. Macco, B.; Bivour, M.; Deijkers, J. H.; Basuvalingam, S. B.; Black, L. E.; Melskens, J.; van de Loo, B. W. H.; Berghuis, W. J. H.; Hermle, M.;

Kessels, W. M. M. Effective passivation of silicon surfaces by ultrathin atomic-layer deposited niobium oxide. *Appl. Phys. Lett.* **2018**, *112* (24), 242105. DOI: 10.1063/1.5029346 (acccessed 4/21/2023).

17. Martin, Julia L. Surface Science of Low-Dimensional materials Towards Controlling Chemical and Optoelectronic Structure, Connecting Dissimilar Materials, and Improving Atmospheric Stability. Worcester Polytechnic Institute, **2023**

18. Berube, Abby D. Quantification of the States and Reactivity of Zirconium-based Metal-organic Framework Surfaces with Organosilanes. Worcester Polytechnic Institute, **2023**

19. Hu, M.; Luber, E. J.; Buriak, J. M. Reconsidering X-ray Photoelectron Spectroscopy Quantification of Substitution Levels of Monolayers on Unoxidized Silicon Surfaces. *J. Phys. Chem. C* **2020**, *124* (30), 16461–16477. DOI: 10.1021/acs.jpcc.0c04101.

20. Mendes, J. L. Interfacial States, Energetics, and Passivation of Large-Grain amd Thin-Film Antifluorite Cesium Titanium Bromide. Worcester Polytechnic Institute, **2021**.

21. Mendes, J. L.; Gao, W.; Martin, J. L.; Carl, A. D.; Deskins, N. A.; Granados-Focil, S.; Grimm, R. L. Interfacial States, Energetics, and Atmospheric Stability of Large-Grain Antifluorite Cs_2TiBr_6. *J. Phys. Chem. C* **2020**, *124* (44), 24289–24297. DOI: 10.1021/acs.jpcc.0c08719.